JACS Au
AN OPEN ACCESS JOURNAL OF THE AMERICAN CHEMICAL SOCIETY

pubs.acs.org/jacsau
Article

Generation of Subnanometer Metal Clusters in Silicoaluminate Zeolites as Bifunctional Catalysts

Kun Zhang,† Xiaomeng Dou,† Huaming Hou,† Ziyu Zhou, Miguel Lopez-Haro, Debora M. Meira, Ping Liu, Peng He,* and Lichen Liu*

Cite This: JACS Au 2023, 3, 3213−3226

Read Online

ACCESS | Metrics & More | Article Recommendations | Supporting Information

ABSTRACT: Zeolite-encapsulated subnanometer metal catalysts are an emerging class of solid catalysts with superior performances in comparison to metal catalysts supported on open-structure solid carriers. Currently, there is no general synthesis methodology for the encapsulation of subnanometer metal catalysts in different zeolite structures. In this work, we will show a general synthesis method for the encapsulation of subnanometer metal clusters (Pt, Pd, and Rh) within various silicoaluminate zeolites with different topologies (MFI, CHA, TON, MOR). The successful generation of subnanometer metal species in silicoaluminate zeolites relies on the introduction of Sn, which can suppress the migration of subnanometer metal species during high-temperature oxidation−reduction treatments according to advanced electron microscopy and spectroscopy characterizations. The advantage of encapsulated subnanometer Pt catalysts in silicoaluminate zeolites is reflected in the direct coupling of ethane and benzene for production of ethylbenzene, in which the Pt and the acid sites work in a synergistic way.

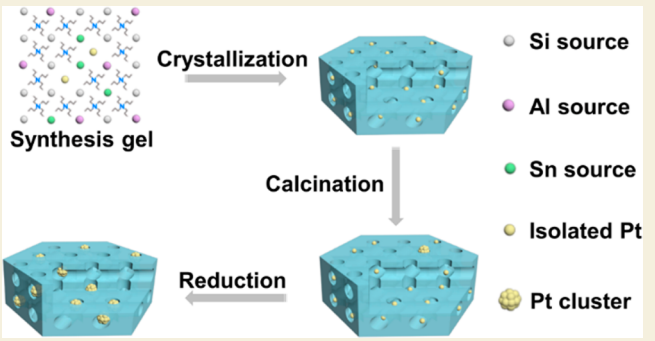

KEYWORDS: *silicoaluminate zeolites, subnanometer metal clusters, alkane activation, platinum, tin*

INTRODUCTION

Encapsulation of subnanometer metal entities (single metal atoms and metal clusters made by a few atoms) within zeolites is an emerging class of supported metal catalysts which exhibit unique catalytic properties in comparison with the conventional metal nanoparticles supported on open-structure carriers.[1−3] On one hand, the subnanometer metal species expose more active sites than nanoparticles with sizes of >1 nm. Especially, the subnanometer metal species can provide more under-coordinated metal sites, which may offer markedly higher reactivity than the well-coordinated metal sites.[4,5] On the other hand, the stability of the encapsulated metal species in zeolite structures will be greatly improved due to the spatial confinement of the microporous channels/cavities.[6,7] In particular, for reactions that require high temperatures, such as dehydrogenation of light alkanes, dehydroaromatization and hydroisomerization of alkanes, the enhanced resistance to sintering can considerably prolong the operating life of the metal catalysts.[8]

In the past years, several synthesis methods have been proposed for the encapsulation of subnanometer metal catalysts within zeolites via one-pot synthesis approaches or postsynthesis treatments.[9−11] It should be noted that most of the successful examples for stabilization of subnanometer metal clusters are achieved with pure-silica zeolites. In the case of metal particles encapsulated in silicoaluminate zeolites, the particle sizes are mostly larger than 1 nm,[12−18] which could be caused by the different crystallization conditions and electronic properties of the zeolite frameworks due to the presence of aluminum.[19] Currently, about 50 of the total >200 zeolite topological structures can be synthesized as pure-silica forms according to the database of the International Zeolite Association while the majority of zeolite topological structures can only be synthesized with the doping of other heteroatoms, such as Al, Ge, P etc.[20,21] Metal-modified silicoaluminate zeolites also offer the possibility of constructing bifunctional catalysts with metal sites and zeolite acid sites for practical processes. For instance, Ir/Beta and Pt/ZSM-22 catalysts are used in industrial processes for the catalytic ring-opening reaction of decalin and branched alkanes as well as the hydroisomerization of linear alkanes, respectively.[22,23] Therefore, from both fundamental and practical points of view, it is crucial to develop synthesis methodologies for the generation

Received: September 18, 2023
Revised: October 7, 2023
Accepted: October 9, 2023
Published: November 2, 2023

https://doi.org/10.1021/jacsau.3c00548
JACS Au 2023, 3, 3213−3226

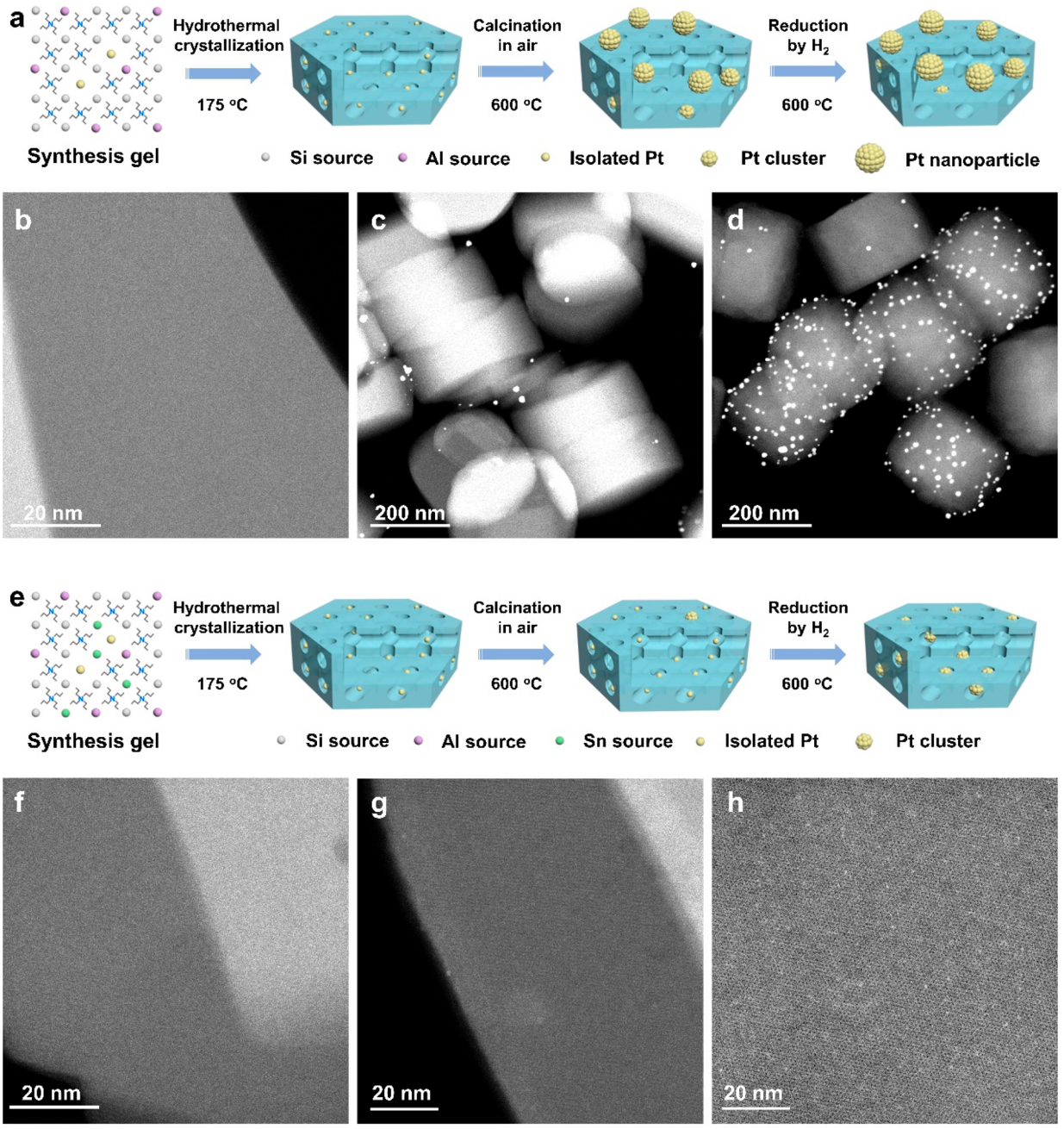

Figure 1. Generation and stabilization of subnanometer Pt clusters within ZSM-5 zeolite structure. (a) Illustration of the evolution of Pt species in different stages of the preparation of K-Pt-ZSM5 sample. (b) K-Pt-ZSM5-AS sample obtained after hydrothermal crystallization, (c) K-Pt-ZSM5-Air sample obtained after calcination in air at 600 °C, and (d) K-Pt-ZSM5 sample obtained after reduction by H_2 at 600 °C. (e) Illustration of the evolution of Pt species in different stages of the preparation of the K-PtSn-ZSM5 sample. (f) K-PtSn-ZSM5-AS sample obtained after hydrothermal crystallization, (g) K-PtSn-ZSM5-Air sample obtained after calcination in air at 600 °C, and (h) K-PtSn-ZSM5 sample obtained after reduction by H_2 at 600 °C.

and stabilization of subnanometer clusters within silicoaluminate zeolites to expand the library of zeolite-encapsulated metal materials for applications in catalysis.

In this work, we will show a general synthesis method for the encapsulation of subnanometer metal clusters (Pt, Pd, Rh) within various silicoaluminate zeolites with different topologies (MFI, CHA, TON, MOR). The successful generation of subnanometer metal species in silicoaluminate zeolites relies on the introduction of Sn species into metal-silicoaluminate zeolites, and the subnanometer Pt clusters encapsulated in silicoaluminate zeolite exhibit enhanced performance in the direct coupling reaction of ethane and benzene for production of ethylbenzene compared to Pt nanoparticles in ZSM-5 or Pt clusters encapsulated in pure-silica zeolite.

RESULTS AND DISCUSSION

Encapsulation of Subnanometer Pt Clusters within ZSM-5

As shown in our prior work, subnanometer Pt clusters can be generated in pure-silica MFI zeolite by employing tetrapropylammonium hydroxide (TPA^+OH^-) as the organic structure-directing agent (OSDA) and adding alkaline metal (K^+) to

https://doi.org/10.1021/jacsau.3c00548
JACS Au 2023, 3, 3213−3226

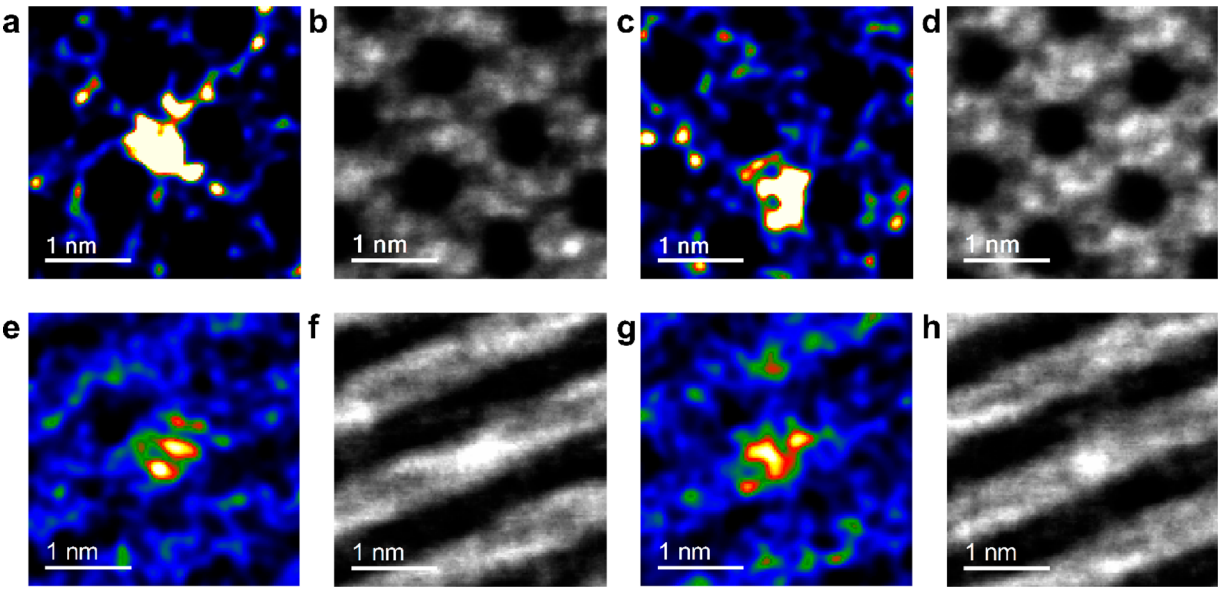

Figure 2. Determination of the location of subnanometer Pt clusters in the K-PtSn-ZSM5 sample. (a, c) HAADF-STEM images and (b, d) iDPC-STEM images along the [010] orientation. (e, g) HAADF-STEM images and (f, h) iDPC images along the tilted-[010] orientation. The paired HAADF-STEM and iDPC-STEM images were acquired in the same area but with different imaging modes.

stabilize the Pt species against sintering during high-temperature oxidation and reduction treatments.[7,24] Herein, we attempt to extend the synthesis method to the generation of Pt clusters in silicoaluminate zeolites, which are more widely used in practical applications than their pure-silica counterparts. We conducted the synthesis of Pt-modified ZSM-5 (denoted as K-Pt-ZSM5) by following the reported method with K^+ as the promotor, because the Pt-ZSM5 sample prepared under K-free condition contained large Pt nanoparticles (Figures S1 and S2). The X-ray diffraction (XRD) pattern of the resultant K-Pt-ZSM5 sample (with a Pt loading of ∼0.42 wt % and Si/Al ratio of ∼49, determined by ICP-OES, as shown in Table S1) shows typical diffraction peaks corresponding to MFI zeolite (Figure S3). The evolution of Pt species during the three key stages in the one-pot synthesis of metal-zeolite materials, i.e., hydrothermal crystallization, calcination in air to remove OSDA, and reduction by H_2 to obtain metallic Pt clusters, has been tracked by high-angle angular dark-field scanning transmission electron microscopy (HAADF-STEM). As shown in Figures 1a−d and S4−S6, neither metal clusters nor nanoparticles can be visualized in the HAADF-STEM images of the as-synthesized K-Pt-ZSM5 sample (named as K-Pt-ZSM5-AS) obtained from hydrothermal crystallization (see Figures 1b and S4), indicating that the Pt species should be atomically dispersed in the zeolite crystallites. However, Pt nanoparticles with diameters of 3−10 nm are observed on the external surface of the zeolite crystallites upon calcination (K-Pt-ZSM5-Air sample, shown in Figures 1c and S5), suggesting that the presence of Al species in the zeolite framework is detrimental for the stabilization of subnanometer Pt clusters in ZSM-5 crystallites. This result is in sharp contrast to the behavior observed with pure-silica MFI zeolite, in which subnanometer Pt species remain stabilized after calcination treatment.[7] After reduction by H_2 at 600 °C, the Pt nanoparticles were further aggregated into larger ones (K-Pt-ZSM5 sample, shown in Figures 1d and S6). As revealed by theoretical studies, the stabilization of subnanometer Pt species within the microporous channels is strongly related to the electronic properties of the anchoring site provided by the zeolite framework.[25,26] The incorporation of Al into the zeolite framework modifies the charge properties of the zeolite framework,[27] altering the interaction between the Pt atoms and the ZSM-5 framework and thus causing the formation of Pt nanoparticles instead of subnanometer Pt species.

Based on the electron microscopy characterization results, it is inferred that the stabilization of Pt species during the calcination treatment could be a critical issue because of the high mobility of Pt species in oxidative atmosphere at elevated temperatures.[28,29] Given the high affinity of oxidized Pt species to reducible metal oxides (such as CeO_2, TiO_2, and SnO_2), incorporating SnO_2 species into ZSM-5 zeolite structure may suppress the migration and sintering of Pt species during the high-temperature calcination treatment.[29−32] Motivated by the hypothesis, we synthesized K-PtSn-ZSM5 samples via a one-pot approach, in which $SnCl_4{\cdot}5H_2O$ was added into the synthesis gel as a Sn precursor. The crystalline structure and chemical composition of K-PtSn-ZSM5 sample were analyzed using XRD and ICP-OES, respectively, as shown in Figure S3 and Table S1. The MFI-type structure remains intact after the introduction of Sn, and the Pt loading and Si/Al ratio in the final K-PtSn-ZSM5 material are similar to those of K-Pt-ZSM5. As shown in the electron microscopy characterization results, the introduction of Sn into the synthesis gel did not influence the dispersion of Pt species in the as-synthesized K-PtSn-ZSM5-AS sample derived from hydrothermal crystallization (Figures 1f and S7). More importantly, Pt species remain highly dispersed after calcination in air at 600 °C (Figures 1g and S8). After reduction treatment by H_2 at 600 °C, subnanometer Pt clusters with good dispersion within the ZSM-5 zeolite crystallites are formed, as visualized in the HAADF-STEM images (Figures 1h and S9). Accordingly, it can be concluded the addition of Sn does not interfere with the crystallization of the ZSM-5 zeolite and can effectively stabilize subnanometer Pt species during the high-temperature calcination and reduction treatments, thus avoiding the sintering of Pt into nanoparticles. It should be noted that, in

https://doi.org/10.1021/jacsau.3c00548
JACS Au 2023, 3, 3213−3226

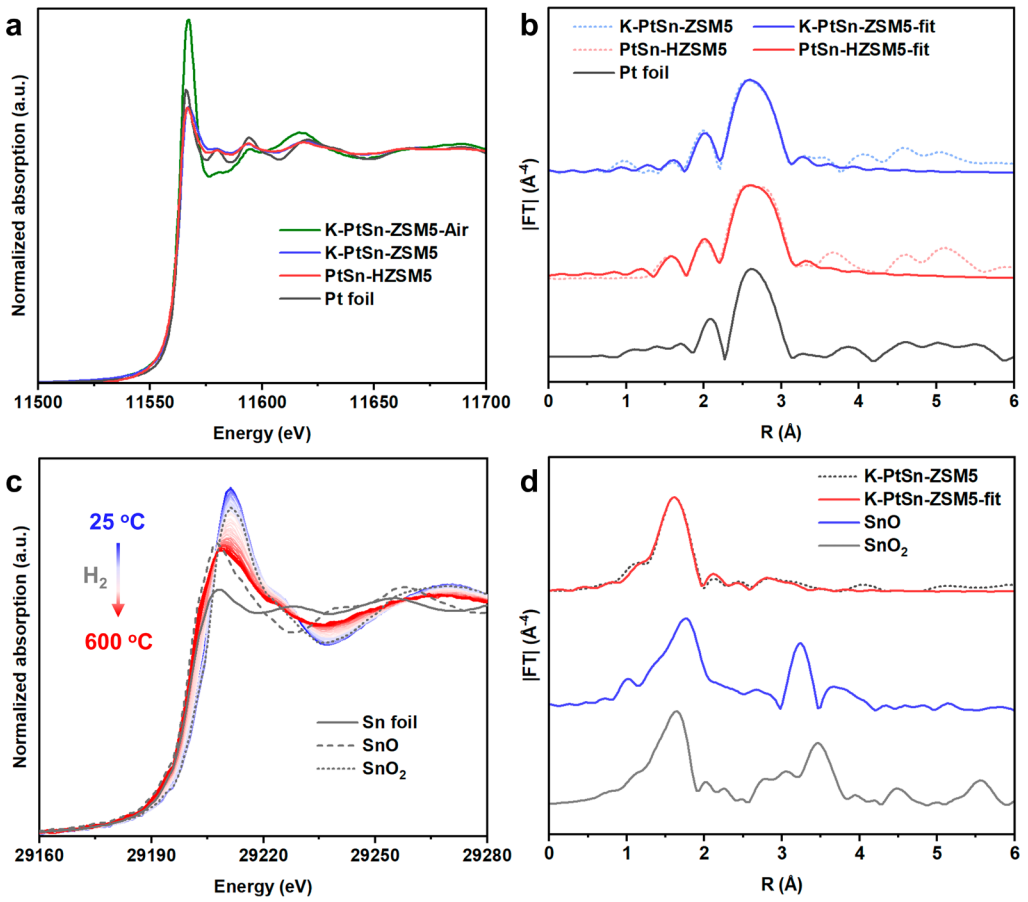

Figure 3. Characterization of K-PtSn-ZSM5 by X-ray absorption spectroscopy. (a) XANES spectra of the Pt L_3-edge of the K-PtSn-ZSM5-Air sample obtained after calcination in air, the K-PtSn-ZSM5 sample obtained after reduction by H_2, and the PtSn-HZSM5 sample obtained after ion-exchange treatment. The Pt L_3-edge XANES spectrum of Pt foil is included as reference. (b) EXAFS spectra of Pt L_3-edge of K-PtSn-ZSM5 sample obtained after reduction by H_2, the PtSn-HZSM5 sample obtained after ion-exchange treatment, and the reference Pt foil. (c) In situ Sn K-edge XANES spectra of K-PtSn-ZSM5 obtained from 25 to 600 °C during the reduction treatment by H_2. The Sn K-edge XANES spectra of Sn foil, SnO and SnO_2 are included as reference. (d) Sn K-edge EXAFS spectra of the K-PtSn-ZSM5 sample after reduction, SnO, and SnO_2.

order to ensure the successful generation and stabilization of Pt clusters, it is necessary to introduce both K and Sn in the synthesis mixture, as indicated by the formation of large Pt particles in the K-free PtSn-ZSM5 samples (Figures S10 and S11).

To validate the successful encapsulation of the Pt clusters in the ZSM-5 zeolite structure in the K-PtSn-ZSM5 sample, the hydrogenation of olefins with distinct kinetic diameters was conducted. Ethene (kinetic diameter of ca. 0.39 nm) and *cis*-cyclooctene (kinetic diameter of ca. 0.79 nm) were used as the model compounds for testing the encapsulation efficiency of Pt species in ZSM-5 zeolite structure, which gives a pore size of ca. 0.55 nm. The hydrogenation of *cis*-cyclooctene should be catalyzed by Pt sites on the external surfaces of ZSM-5, while ethene can access the active Pt sites both encapsulated within ZSM-5 and located on external surfaces. The successful encapsulation of Pt species in the K-PtSn-ZSM5 sample is confirmed by comparing the relative reaction rates of the two substrates and comparison with a reference $PtSn/SiO_2$ catalyst (see Figure S12 and Table S2).[13,16,17]

It can be expected that the surrounding environment of the metal species confined within zeolite structures will affect their physicochemical properties. In this sense, it is very important to figure out the spatial distribution of the encapsulated subnanometer metal species in the zeolite matrix. The location of the subnanometer Pt clusters within zeolite crystallites in the K-PtSn-ZSM5 sample has been studied by the combination of HAADF-STEM and integrated differential phase contrast (iDPC-STEM) imaging techniques.[33] The former is particularly sensitive to heavy elements, such as Pt in this work, and the latter enables clear imaging of the zeolite framework structure. The precise location of the subnanometer Pt clusters can therefore be accurately determined by correlating the two images obtained in the same area but in two different modes. As displayed in the iDPC image along the [010] orientation (Figure 2b, d), the framework of the ZSM-5 zeolite (bright area in the images) and the 10-ring straight channels (black area in the image) can be clearly observed. In paired HAADF-STEM images (Figure 2a, c), brighter spots with sizes of ~0.5 nm are attributed to subnanometer Pt clusters, which are mainly located in the sinusoidal 10-ring channels, rather than the straight channels or intersectional voids. The selective generation of Pt clusters in the sinusoidal 10-ring channels is also confirmed by the paired HAADF-STEM and iDPC-STEM images along the tilted-[010] orientation (Figure 2e–h), because the Pt clusters (visualized in the HAADF-STEM images) overlap with the 10-ring sinusoidal channels (visualized in the iDPC images).

We characterized the as-synthesized K-PtSn-ZSM5-AS sample to understand the regioselective location of Pt clusters

https://doi.org/10.1021/jacsau.3c00548
JACS Au 2023, 3, 3213–3226

Table 1. Fitting Results of Pt L_3-Edge and Sn K-Edge EXAFS Spectra[a]

samples	path	distance	CN	σ^2	ΔE_0	*R*-factor
K-PtSn-ZSM5	Pt−Pt	2.75(1)	6.4(8)	0.006(1)	4.2(13)	3.0%
	Sn−O	2.06(0)	3.1(1)	0.005(1)	9.8(5)	0.3%
PtSn-HZSM5	Pt−Pt	2.76(1)	6.4(4)	0.005(3)	6.1(10)	1.3%

[a]CN, coordination number; σ^2, Debye−Waller factor; ΔE_0, inner potential correction; *R*-factor, difference between modeled and experimental data. For the fit of the Pt L_3-edge EXAFS spectrum, S_0^2 was fixed as 0.82, which was obtained from Pt foil. Data range: $3.5 \le k \le 13$ Å^{-1}, $1.3 \le R \le 3.2$ Å. The number of variable parameters is 6, out of a total of 10.3 ($2\Delta k\Delta R/\pi$) independent data points. For the fit of Sn K-edge EXAFS spectrum, S_0^2 was fixed as 1.0, which was obtained from SnO_2 sample. Data range: $3.0 \le k \le 12.5$ Å^{-1}, $1.0 \le R \le 2.5$ Å. The number of variable parameters is 4, out of a total of 8.8 ($2\Delta k\Delta R/\pi$) independent data points.

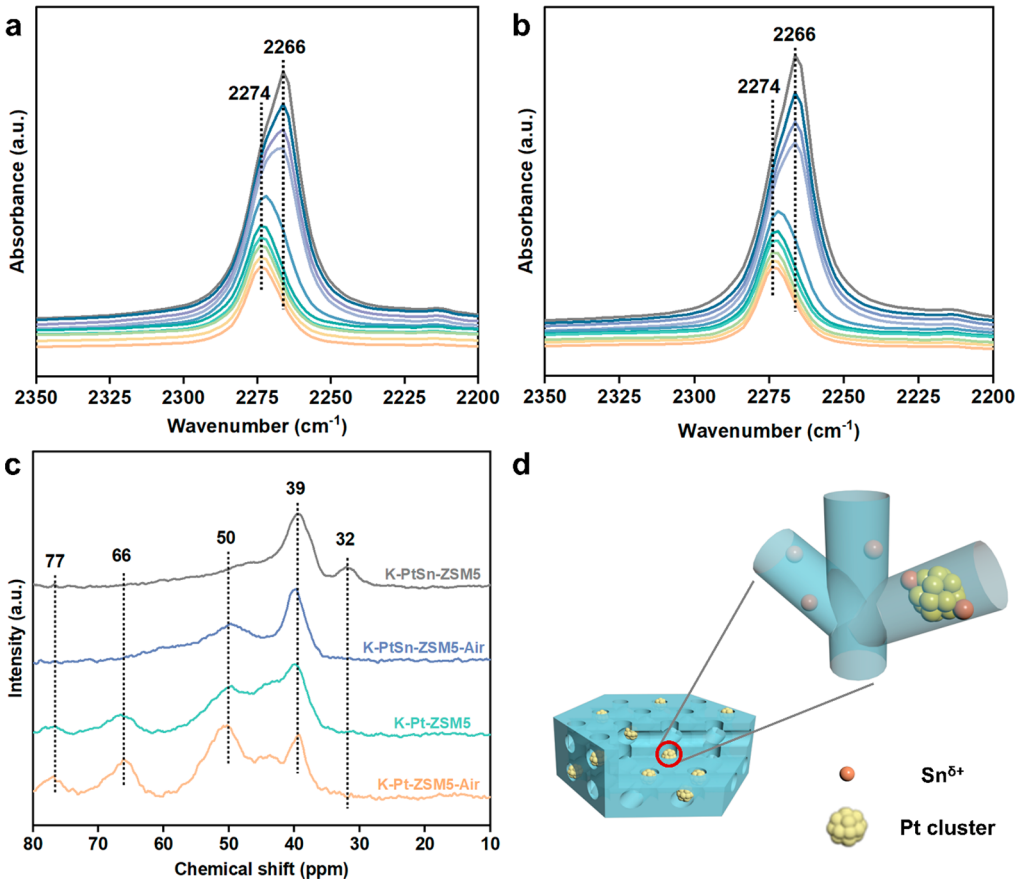

Figure 4. Spectroscopy characterizations of Sn species in K-PtSn-ZSM5. (a, b) IR spectra of CD_3CN adsorbed on K-PtSn-ZSM5 after calcination in air (a) and reduction by H_2 (b). (c) ^{31}P solid state NMR spectra of TMPO adsorbed on K-Pt-ZSM5 and K-PtSn-ZSM5 samples after calcination in air (K-Pt-ZSM5-Air and K-PtSn-ZSM5-Air) and after reduction by H_2 (K-Pt-ZSM5 and K-PtSn-ZSM5). (d) Schematic illustration of the structural features of Pt clusters and Sn species in the K-PtSn-ZSM5 material.

in the ZSM-5 zeolite. According to the high-resolution HAADF-STEM images of the K-PtSn-ZSM5-AS sample (see Figure S13), the Pt species should exist as atomically dispersed species within the ZSM-5 structure. Based on the thermogravimetry (TG) (Figure S14) and elemental analysis results, the number of the OSDA molecules (i.e., TPA^+OH^-) per unit cell of the MFI structure was estimated at approximately 4.1 for K-PtSn-ZSM5-AS (Table S3), which corresponds to the four intersectional voids within each unit cell.[34] Therefore, the atomically dispersed Pt species should not be able to occupy the intersectional voids due to the full occupancy by the OSDA molecules in the K-PtSn-ZSM5-AS sample. Besides, possibly due to the fact that the sinusoidal channels have more space to accommodate the Pt and Sn precursors compared to the straight channels (Figure S15), the metal species are stabilized within the sinusoidal channels.[35]

To follow the formation process of subnanometer Pt clusters, in situ spectroscopic techniques are employed to probe their electronic and coordination environment. The X-ray absorption near edge structure (XANES) spectra (Figure 3a) show that Pt species are in the oxidized state after calcination in air at 600 °C. After being reduced by H_2 at 600 °C, the white-line intensity decreases to a state close to the reference Pt foil, indicating that Pt species should be in metallic state in the final K-PtSn-ZSM5 material. The binding energies at 331.6 and 314.7 eV shown in Figure S16 can be assigned to $4d_{3/2}$ and $4d_{5/2}$ of Pt^0, respectively.[36] The weak signal of the Pt 4d XPS spectra infers the encapsulation of the Pt species in ZSM-5 crystallites. The coordination environment of Pt species in K-PtSn-ZSM5 upon reduction by H_2 at 600 °C has been studied by Pt L_3-edge extended X-ray absorption fine structure (EXAFS) spectroscopy (Figure 3b).

https://doi.org/10.1021/jacsau.3c00548
JACS Au 2023, 3, 3213−3226

The fitting results (Table 1) show that only the Pt−Pt bonding is observed while the Pt−O and Pt−Sn bonds are absent, indicating that Pt species are metallic and Pt−Sn alloys are not formed. The coordination number of Pt−Pt bonding further confirms the formation of subnanometer Pt clusters in the K-PtSn-ZSM5 sample, being consistent with the electron microscopy observations.

The chemical states of Sn species in the K-PtSn-ZSM5 material during the synthesis procedure are studied by in situ XANES (Figure 3c). The Sn species in the K-PtSn-ZSM5-Air sample obtained after calcination in air are Sn^{4+} species. During the reduction treatment by H_2, a gradual decrease of the white-line intensity is observed along the increasing temperature from 25 to 600 °C. By comparison with the reference SnO_2, SnO and Sn foil, it is inferred that the Sn species remain in partially reduced state (denoted $Sn^{\delta+}$) after reduction treatment at 600 °C. The presence of partially reduced Sn species instead of metallic Sn species in the final K-PtSn-ZSM5 material is also supported by the Sn 3d region XPS spectra (Figure S17).[37] Only Sn−O bonding is observed in the Sn K-edge EXAFS spectra of the K-PtSn-ZSM5 sample, while the Sn−Sn and Pt−Sn bonds are absent (Figure 3d). Additional higher-shell Sn−O−Sn bonding is not observed either, indicating that Sn species are well dispersed within the K-PtSn-ZSM5 sample, probably in the form of isolated $Sn^{\delta+}$ species or tiny SnO_x clusters. The absence of Pt−Sn interaction in the Pt L_3-edge and Sn K-edge EXAFS spectra could be related to the low abundance of Pt−Sn or Pt−O−Sn bonding in the K-PtSn-ZSM5 sample (see discussion in Supplementary Note 1 in the Supporting Information).

We employed spectroscopy techniques to characterize the interaction between Sn species and the probe molecules to figure out the location of Sn species in the K-PtSn-ZSM5 sample. The IR spectra of CD_3CN adsorbed on oxidized and reduced K-PtSn-ZSM5 samples are shown in Figure 4a and b, respectively. The stretching bands of C≡N of CD_3CN adsorbed on Si−OH (2274 cm^{-1}) and physiosorbed by the zeolite (2266 cm^{-1}) are observed, while the vibrational frequencies attributed to CD_3CN adsorbed on isolated framework Sn sites (typically located at 2316 and 2308 cm^{-1}) are not detected, indicating the absence of Sn incorporated in the ZSM-5 framework.[38] Moreover, the position of Sn atoms was also investigated by solid state ^{31}P NMR spectroscopy with trimethylphosphine oxide (TMPO) as the probe molecule. As depicted in Figure 4c, the NMR signals at 39 and 32 ppm correspond to the physiosorbed TMPO.[39] For the K-Pt-ZSM5 sample, two peaks at 66 and 77 ppm are assigned to TMPO interacting with Brønsted acidic sites,[40] which remain after reduction treatment by H_2. However, these peaks were not observed in the spectra of K-PtSn-ZSM5, suggesting that the addition of Sn can neutralize a considerable portion of the Brønsted acid sites in ZSM-5. The NMR peak at 50 ppm corresponds to TMPO interacting with extra-framework Lewis acidic sites.[41] The signals of TMPO interacting with framework Sn sites are expected in the range between 55 and 60 ppm,[42] which are not observed with the oxidized and reduced K-PtSn-ZSM5 sample, inferring the absence of framework Sn species in ZSM-5 zeolite. These results are in line with the reported works which show the feasible incorporation of Sn into the framework of large-pore zeolites (such as Beta zeolite) but not in medium-pore zeolites (such as ZSM-5), due to the larger atomic radius of Sn than Si.[38,43]

We have characterized the location of the Al species in three samples (K-PtSn-ZSM5, K-Pt-ZSM5, and K-ZSM5) by ^{27}Al NMR spectroscopy. As shown in Figure S18, the three samples exhibit quite similar ^{27}Al NMR spectra, as suggested by the fitting results shown in Table S5. Moreover, by comparing our results and the related literature, it is suggested that the Al species should be randomly distributed in the ZSM-5 zeolite, occupying both the intersections and the straight/sinusoidal channels.[34]

Understanding the Stabilization Effect of Sn to Pt Species

A series of K-PtSn-ZSM5 samples with different Sn contents were prepared to reveal the stabilization effect of Sn on Pt species within the ZSM-5 zeolite. Two samples with lower Sn contents (0.24 and 0.54 wt % of Sn in K-$PtSn_{0.24}$-ZSM5 and K-$PtSn_{0.54}$-ZSM5, respectively) were synthesized via the same one-pot synthesis method as the K-PtSn-ZSM5 sample except for adding different amounts of Sn precursor (Table S1). A gradual increase of the number of Pt clusters is observed with increased Sn content from K-Pt-ZSM-5 to K-$PtSn_{0.24}$-ZSM5 and K-$PtSn_{0.54}$-ZSM5 (Figure S19−S20), indicating that a sufficient amount of Sn is required to guarantee the formation of subnanometer Pt species in ZSM-5. However, as shown in Figure S21, the introduction of an excess amount of Sn will partly inhibit the crystallization of ZSM-5, resulting in the formation of amorphous domains in the sample and the formation of large Pt particles due to insufficient encapsulation of Pt species.

Because the aggregation of Pt in the absence of Sn occurs during the calcination step, we have collected the IR spectra of PtSn-ZSM5 samples with different Sn contents obtained after calcination in air to investigate the effect of Sn on the zeolite structure. As shown in Figure S22, IR bands corresponding to external silanol groups (3743 cm^{-1}), internal silanol groups (3728 and 3693 cm^{-1}) and silanol nests (3500 cm^{-1}) are observed.[44] For the K-Pt-ZSM5 sample, a band at 3593 cm^{-1} was also observed, which could be attributed to the bridging Si-OH-Al, i.e., the Brønsted acidic sites.[45] This band disappears in the Sn-containing samples, implying that Sn can selectively neutralize a great portion of the Brønsted acidic sites in the ZSM-5 zeolite, which is consistent with the observations in the ^{31}P NMR spectra (Figure 4c). The partial neutralization of the Brønsted acidic sites by Sn species could be similar as the behavior of Ga and Zn species in ZSM-5 by forming extra-framework metal species for the replacement of H^+.[46,47] In principle, the neutralization of the −OH groups in ZSM-5 can also be achieved by alkali metals such as K^+. However, even by introducing a double amount of K^+ in the synthesis mixture, Pt nanoparticles are still formed on ZSM-5 (see Figure S23), suggesting that the stabilization of subnanometer Pt species cannot be achieved by solely introducing alkali metals.

The IR spectra show that the amount of internal silanol groups and especially the silanol nests exhibits a significant inverse correlation with the Sn content. On one hand, the concentration of silanol groups is related to the electronic property of the ZSM-5 framework. Replacing the H^+ in the silanol groups with $Sn^{\delta+}$ can enhance the charge density of the O atom, which could be beneficial for binding the positively charged Pt species formed during the calcination procedure via the stronger Pt−O−Sn interaction than the Pt−O−Al or Pt−O−Si interactions.[48] Consequently, the interaction between oxidized Pt species and the zeolite support can be greatly promoted, as supported by the better dispersion of Pt species

https://doi.org/10.1021/jacsau.3c00548
JACS Au 2023, 3, 3213−3226

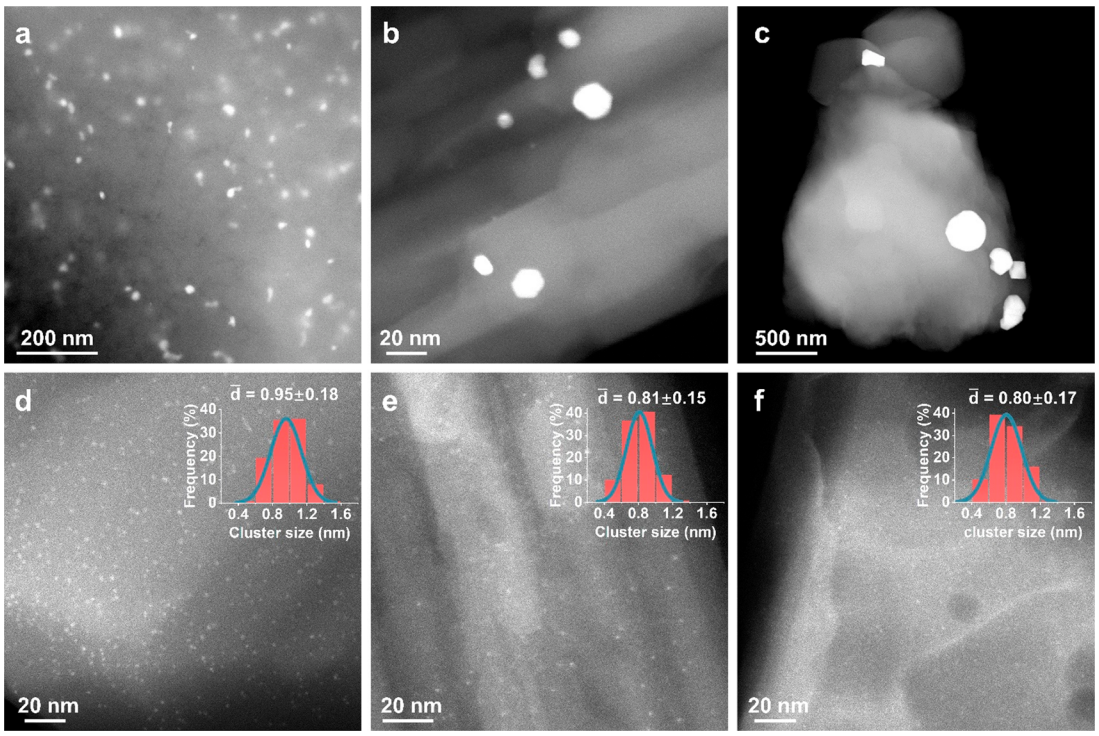

Figure 5. HAADF-STEM images of Pt-zeolite materials with other topological structures. (a) Na-Pt-CHA, (b) K-Pt-TON, (c) Na-Pt-MOR, (d) Na-PtSn-CHA, (e) K-PtSn-TON, and (f) Na-PtSn-MOR. Particle size distribution of Pt in Na-PtSn-CHA, K-PtSn-TON, and Na-PtSn-MOR are embedded in corresponding HAADF-STEM images, respectively.

in the K-PtSn$_x$-ZSM5-Air samples with higher Sn contents (Figures S5, S24, S25, S8), leading to stabilized subnanometer Pt species during calcination and the formation of subnanometer Pt clusters after subsequent reduction by H_2, as illustrated in Figure 4d. On the other hand, the amount of silanol groups reflects the structural integrity of the ZSM-5 crystallites, which could be detrimental for stabilizing the subnanometer Pt species during high-temperature oxidation−reduction treatments, because the sintering of Pt may occur as a result of the migration along the defects in the zeolite channels.

Extending the Synthesis Strategy to Other Silicoaluminate Zeolites

The profound stabilization effects of Sn on subnanometer Pt species in ZSM-5 encourage us to explore such effects in the generation of subnanometer metal species in other silicoaluminate zeolites. By properly adjusting the composition (Si/Al atomic ratios, amount of alkali metals, and the promoter metals), we are able to synthesize metal-zeolite materials with highly stable metal clusters in the microporous channels/cavities. Three types of silicoaluminate zeolites (CHA-type zeolite with 8-ring pores, TON-type zeolite with 10-ring pores and MOR-type zeolite with 12-ring pores) with different topological structures were selected to demonstrate the application scope of our synthesis method. First, we have prepared a series of Pt-zeolite samples by one-pot synthesis approach (see Figure S26 for the XRD patterns). As demonstrated with the HAADF-STEM images (Figures 5a−c and S27−S29), Pt nanoparticles (>2 nm) on the external surface of zeolites are formed in all the samples, indicating the unsuccessful encapsulation of Pt clusters in the zeolite crystallites. Notably, after the introduction of Sn species, the dispersion of Pt species in the final PtSn-zeolite materials can be greatly improved, and subnanometer Pt clusters with uniform distribution within the silicoaluminate zeolite crystallites can be confirmed in the HAADF-STEM images (Figures 5d−f and S30−S32). The encapsulation efficiencies of Pt species in different PtSn-zeolite samples have also been evaluated by hydrogenation reactions of ethylene and *cis*-cyclooctene, which infer the encapsulation of Pt species in the silicoaluminate zeolite crystallites according to the measured relative reaction rates (see Table S2).

In addition to encapsulation of subnanometer Pt clusters in silicoaluminate zeolites, we have also attempted to extend the synthesis methodology for generation and stabilization of other noble metal clusters in ZSM-5. As shown in Figures S33−S36, the addition of Sn can also greatly improve the dispersion of Rh and Pd in ZSM-5, resulting in the formation of subnanometer Pd and Rh clusters in ZSM-5 zeolite crystallites. These results indicate that, the employment of an oxyphilic metal as an addictive could be a general strategy to form subnanometer metal clusters in silicoaluminate zeolites.

Ion-Exchange Treatment with PtSn-Zeolite Materials

In order to liberate the acid sites within the Pt-zeolite materials, we performed ion-exchange treatments to replace the alkali metals with H^+. After the ion-exchange treatment, the good dispersion of Pt species in the PtSn-HZSM5 sample is maintained, as suggested by the HAADF-STEM images in Figure 6 and the EXAFS characterization results (Figure 3 and Table 1). The location of the subnanometer Pt clusters also remains unchanged according to the paired HAADF-STEM and iDPC-STEM images, indicating the structural robustness of the Pt clusters confined in the 10-ring channels. The subnanometer Pt clusters remain stable after two cycles of consecutive high-temperature oxidation−reduction treatment (Figure S37). By substitution of the alkali metals with H^+, the

https://doi.org/10.1021/jacsau.3c00548
JACS Au 2023, 3, 3213−3226

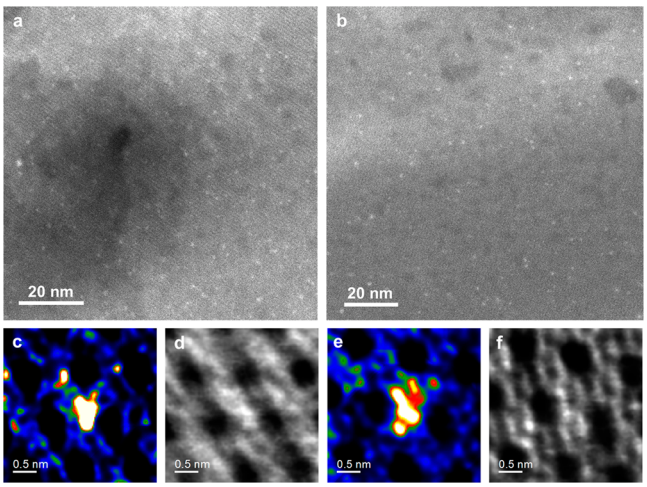

Figure 6. Structural characterizations of the PtSn-HZSM5 sample obtained after ion exchange. (a, b) Low-magnification HAADF-STEM images of the PtSn-HZSM5 sample. (c–f) Determination of the location of Pt clusters in ZSM-5 zeolite by paired HAADF-STEM (c, e) and the corresponding iDPC-STEM images (d, f).

acid sites in the ZSM-5 framework become available, as confirmed by the pyridine-IR spectra (Figure S38). In comparison with the monometallic Pt-HZSM5, the PtSn-HZSM5 exhibits slightly fewer acid sites, which could be caused by the interaction between Sn species and the ZSM-5 framework. Additionally, the uniform distribution of Pt clusters in other silicoaluminate zeolites is preserved after ion-exchange treatments (Figures S39–S41), suggesting that the synthesis strategy can be extended for the preparation of a variety of bifunctional catalysts with both metal and acid sites in different zeolite structures.

Catalytic Performance of PtSn-ZSM5 Catalysts

The direct coupling of ethane and benzene allows the production of ethylbenzene in a single-step process instead of the two separated processes in current chemical industry.[49,50] As illustrated in Figure 7a, the direct coupling reaction between ethane and benzene can be considered as a tandem process catalyzed by the metal sites (for dehydrogenation of ethane to ethylene) and the acid sites (for alkylation of benzene with ethylene), respectively. The ethane–benzene coupling reaction is chosen as a model reaction to study the catalytic properties of different Pt-zeolite materials as bifunctional catalysts. For comparison, we have prepared a PtSn-MFI sample by incorporating Pt clusters in pure-silica MFI as a reference catalyst to study the influence of acid sites (see characterization results in Figure S42).[7] As shown in Figure 7b, the PtSn-MFI catalyst exhibits low initial activity (0.2% conversion of ethane) and ineffectiveness for conversion of benzene. According to the isotopic exchange experiments with C_2H_6 and D_2, PtSn-MFI has good capability for activation of C–H bonds in ethane (Figure S43). Therefore, the ineffectiveness for the production of ethylbenzene should be attributed to the absence of acid sites (Figure S38 and Table S4). In addition, low conversion of ethane is limited by the thermodynamic equilibrium of the ethane dehydrogenation reaction at 400 °C, because it is a highly endothermic reaction. After physically mixing the PtSn-MFI catalyst with the HZSM5 (ZSM-5 in H-form), we can observe an increase in conversions of ethane and benzene and the formation of ethylbenzene. The enhanced activity is ascribed to the coupling reaction between ethylene and benzene catalyzed by acid sites in HZSM5, which greatly promotes the ethane dehydrogenation reaction on Pt sites by continuously consuming the ethylene. Furthermore, we have tested the performance of the Pt-HZSM5 catalyst prepared by one-pot synthesis and it shows better performance than the physical mixture of PtSn-MFI and HZSM5, indicating that the direct coupling reaction is favorable when increasing the proximity of the metal and acid sites. More interestingly, the PtSn-HZSM5 catalyst exhibits even higher activity than the Pt-HZSM5, whose conversions of ethane and benzene are nearly two times of those obtained with the Pt-HZSM5 catalyst. The PtSn-HZSM5 catalyst shows a superior production rate of ethylbenzene in comparison with the reported systems (Table S6).

According to the catalytic results obtained with different Pt-zeolite catalysts and the PtSn-HZSM5 catalysts with different Sn loadings (Figures S43 and S44), the impacts of Sn species on the catalytic properties can be reflected in the following three aspects. First, the introduction of Sn can stabilize the subnanometer Pt clusters, which should have significant advantages over Pt nanoparticles for activation of light alkanes, because the activation of C–H bonds is more favorable on under-coordinated Pt sites than that on well-coordinated Pt sites. Therefore, the PtSn-HZSM5 catalyst has higher capability for dehydrogenation of ethane to ethylene, which is also confirmed by the isotopic exchange experiments with C_2H_6 and D_2 (Figure S43). Second, similar to the effects observed with dehydrogenation of light alkanes, the interaction between Pt and Sn can suppress the coke formation on Pt sites and the undesired breaking of C–C bonds, resulting in the extended catalyst lifetime (Figure 7d) and declined selectivity to methane (Figure 7c) of PtSn-HZSM5 in comparison with Pt-HZSM5. Third, the presence of Sn in the PtSn-HZSM5 will neutralize a portion of the acid sites in the HZSM5 zeolite (Figure S38 and Table S4), but the influences of Sn species on the catalytic performances for direct coupling of the ethene intermediate and benzene are minor according to the catalytic results shown in Figure S45. The decreased acidity of HZSM5 zeolite after the introduction of Sn species may also contribute to the improved long-term stability (Figure 7d-e) by mitigating the coke deposition because heavy aromatics (precursors of coke) tend to form on the sites with strong acidity, as inferred by the characterizations of the spent catalysts (Figures S46 and S47). The structural robustness of the spent PtSn-HZSM5 catalyst is confirmed by the electron microscopy characterization results (Figures S48–S50).

OUTLOOK

In summary, a general method for encapsulating subnanometer metal clusters within silicoaluminate zeolites has been developed, which can greatly broaden the scope of zeolite materials with the encapsulation of subnanometer metal clusters. In principle, by varying Sn to other oxyphilic metals (such as Zn, Ga, In, Ge etc.), other types of bimetallic or even multimetallic nanoclusters could be formed and stabilized in zeolite structures, which will lead to the generation of a large variety of subnanometer metal catalysts confined in different zeolite structures as bifunctional catalysts.

https://doi.org/10.1021/jacsau.3c00548
JACS Au 2023, 3, 3213–3226

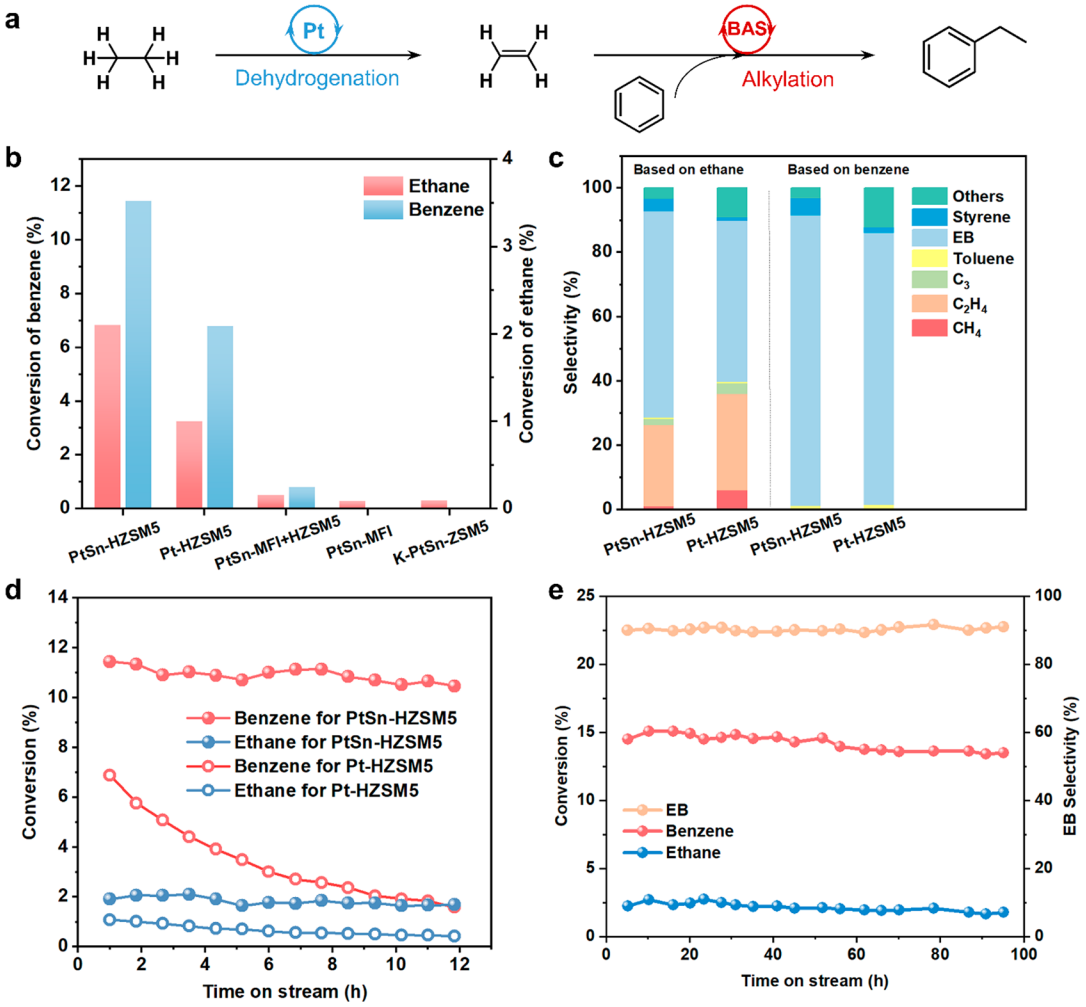

Figure 7. Catalytic performance of alkylation of benzene with ethane on Pt-zeolite catalysts. (a) Illustration of the direct coupling of ethane and benzene via tandem dehydrogenation-alkylation reaction. (b) Initial conversions of benzene and ethane at 1 h. (c) Initial product distributions over PtSn-HZSM5 and Pt-HZSM5 at 1 h based on ethane and benzene, respectively. (d) Conversions of benzene and ethane as a function of reaction time over PtSn-HZSM5 and Pt-HZSM5. (e) Long-term stability test of PtSn-HZSM5. Reaction conditions in plots (b–d) are as follows: 400 °C, atmospheric pressure, ethane/benzene molar ratio of 9 and WHSV of ethane at 2.0 h^{-1}. Reaction conditions in plot (e) are the same as those in plots (b–d), except for the WHSV at 1.2 h^{-1}. "EB" in plot (c) denotes ethylbenzene. "Others" in plot (c) contains xylene, propyl-benzene, diethyl-benzene, and other heavy aromatics.

EXPERIMENTAL SECTION

Materials Synthesis

Synthesis of K-PtSn-ZSM5. The PtSn clusters encapsulated in ZSM-5 zeolite crystallites were synthesized by a one-pot synthesis method, which employed tetraethyl orthosilicate (TEOS) as the Si source, $Al(NO_3)_3{\cdot}9H_2O$ as the Al source, and tetrapropylammonium hydroxide (TPAOH) as the organic structure-directing agent. Batch composition: 1.2 K_2O:16 TPAOH:0.4 Al_2O_3:40 SiO_2:1600 H_2O. First, a TPAOH solution was prepared by mixing 16.24 g of TPAOH (Sigma-Aldrich, 20 wt %, containing ~0.6 wt % of K, product code: 254533-100G) and 12.0 g of distilled water at room temperature. Then, 8.24 g of TEOS (Alfa Aesar, 99+%) was hydrolyzed with TPAOH solution at room temperature for 6 h under stirring (500 rpm). The aluminum source solution was prepared by mixing 0.3 g of $Al(NO_3)_3{\cdot}9H_2O$ (Sinopharm Chemical Reagent Co., Ltd. ≥99.0%) and 3.0 g of distilled water at room temperature. Then the $Al(NO_3)_3$ solution was added dropwise to the TEOS-TPAOH-water mixture, followed by agitation for 3 h. After the addition of aluminum source, 90 mg of $SnCl_4{\cdot}5H_2O$ (Energy Chemical, 99%) was added to the mixture, which was then kept stirring for 30 min. Afterward, 300 μL of H_2PtCl_6 (Sigma-Aldrich, >99.9%) aqueous (0.19 $mol{\cdot}L^{-1}$) and 300 μL of ethylenediamine (Sigma-Aldrich, ≥99%) were added with stirring for another 30 min. The resultant yellow solution was then transferred to Teflon-lined autoclaves and heated in an electric oven at 175 °C for 96 h under static condition. After the hydrothermal process, the solid product was isolated by centrifugation, washed with distilled water and acetone, and then dried at 60 °C. Then the solid sample was calcined under air at 560 °C for 8 h and then at 600 °C for 2 h. Finally, the obtained sample was named as K-PtSn-ZSM5. The K-$PtSn_{0.24}$-ZSM5, K-$PtSn_{0.54}$-ZSM5, and K-$PtSn_{2.33}$-ZSM5 were synthesized by altering the content of $SnCl_4{\cdot}5H_2O$.

Synthesis of K-Pt-ZSM5, K-Sn-ZSM5 and K-ZSM-5. The K-Pt-ZSM5, K-Sn-ZSM5, and K-ZSM-5 samples were prepared by a similar one-pot synthesis as the PtSn-ZSM5. The only difference was that $SnCl_4{\cdot}5H_2O$, H_2PtCl_6 aqueous solution, and both $SnCl_4{\cdot}5H_2O$ and H_2PtCl_6 aqueous solution, respectively, were not added to the synthesis mixture.

Synthesis of Na-PtSn-CHA. Batch composition: 2.6 Na_2O:5.2 RN-OH:1.7 Al_2O_3:50 SiO_2:1100 H_2O. First, 67 mg of NaOH (Sinopharm Chemical Reagent Co., Ltd., AR) was dissolved in 17 g of distilled water at room temperature. Then, 276 mg of $NaAlO_2$ (Shanghai Macklin Biochemical Co., Ltd., AR) was added to the above solution with stirring for 15 min until dissolved. 4.41 g of *N*,*N*,*N*-trimethyl-1-adamantanamonium hydroxide solution (RN-OH, Energy Chemical, 25 wt %) was added with stirring for another 10

https://doi.org/10.1021/jacsau.3c00548
JACS Au 2023, 3, 3213–3226

min. Then, 50 mg of $SnCl_4{\cdot}5H_2O$ and 200 μL of H_2PtCl_6 aqueous (0.19 mol·L^{-1}) and 300 μL of ethylenediamine were added to the resultant solution with stirring for 20 min. 3.03 g of fumed SiO_2 (Degussa, Aerosil 380) was then added to the resultant solution with stirring for 1.5 h. The resultant solution was transferred to Teflon-lined autoclaves and heated in an electric oven at 160 °C for 48 h at 30 rpm. After the hydrothermal process, the solid product was isolated by centrifugation, washed with distilled water and acetone, and then dried at 60 °C. Then the solid sample was calcined under air at 560 °C for 8 h.

Synthesis of K-PtSn-TON. Batch composition: 4.7 K_2O:9.6 DAO:0.35 Al_2O_3:32 SiO_2:1260 H_2O. First, the aluminum source solution was prepared by mixing 235 mg of $Al_2(SO_4)_3{\cdot}18H_2O$ (Sinopharm Chemical Reagent Co., Ltd., AR) and 2.43 g of distilled water, and the KOH solution was prepared by mixing 0.53 g of KOH (Sinopharm Chemical Reagent Co., Ltd., AR) and 2.43 g of distilled water at room temperature. Then, the $Al_2(SO_4)_3$ solution was dropped into the KOH solution under agitation to form a homogeneous solution. A 1,8-diamino-octane solution consisting of 1.39 g of 1,8-diamino-octane (DAO, Innochem, 98%) and 9.7 g of distilled water prepared in advance was dropped into the resultant solution with stirring for 10 min. Then, a silica source solution was prepared by mixing 6.35 g of SiO_2 aqueous (Ludox AS-30, 30 wt %) and 3.59 g of distilled water and added to the resultant solution above with stirring for 30 min. Finally, 30 mg of $SnCl_4{\cdot}5H_2O$, 300 μL of H_2PtCl_6 aqueous (0.19 mol·L^{-1}), and 300 μL of ethylenediamine were added with stirring for 20 min. The resultant yellow solution was then transferred to Teflon-lined autoclaves and kept in an electric oven at 160 °C for 48 h at 30 rpm. After the hydrothermal process, the solid product was isolated by centrifugation, washed with distilled water and acetone and then dried at 60 °C. Then the solid sample was calcined under air at 560 °C for 8 h.

Synthesis of Na-PtSn-MOR. Batch composition: 5.9 Na_2O:1.6 Al_2O_3:30 SiO_2:680 H_2O. First, a NaOH solution was prepared by mixing 0.34 g of NaOH and 0.7 g of distilled water. Then, 0.26 g of $NaAlO_2$ was added to the NaOH solution with stirring until it was dissolved, and 11.5 g of distilled water was added to the resultant solution with stirring. Then, 1.75 g of fumed SiO_2 (Degussa, Aerosil 200) was added to the resultant solution with stirring for 30 min. Finally, 15 mg of $SnCl_4{\cdot}5H_2O$ and 150 μL of H_2PtCl_6 aqueous (0.19 mol·L^{-1}) and 150 μL of ethylenediamine were added with stirring for 20 min. The resultant yellow solution was then transferred to Teflon-lined autoclaves and kept in an electric oven at 170 °C for 24 h under static conditions. After the hydrothermal process, the solid product was isolated by centrifugation, washed with distilled water and acetone and then dried at 60 °C. Then the solid sample was calcined under air at 560 °C for 8 h.

Synthesis of Na-Pt-CHA, K-Pt-TON and Na-Pt-MOR. The Pt-zeolite samples with different topologies were prepared by a one-pot synthesis similar to that of the PtSn-zeolite samples. The only difference was that $SnCl_4{\cdot}5H_2O$ was not added to the synthesis mixture.

Synthesis of PtSn/SiO_2. PtSn/SiO_2 were prepared by a conventional impregnation method. One g of SiO_2 (Sigma-aldrich, surface area of ~550 m^2/g, average pore size of ~6 nm, product code: 227196) was added into 10 g of aqueous solution containing H_2PtCl_6 (3.5 mg of Pt) and $SnCl_4{\cdot}5H_2O$ (13.5 mg of Sn). The solutions were then stirred at room temperature and 300 rpm followed by drying at 80 °C overnight.

Synthesis of K-PdSn-ZSM5. Bimetallic PdSn nanoparticles encapsulated in ZSM5 zeolite with a Si/Al ratio of 50 were prepared by a one-pot synthesis. Batch composition: 1.2 K_2O:16 TPAOH:0.4 Al_2O_3:40 SiO_2:1600 H_2O. First, a TPAOH solution was prepared by mixing 16.24 g of TPAOH (Sigma-Aldrich, 20 wt %, containing ~0.6 wt % of K, product code: 254533-100G) and 12.0 g of distilled water at room temperature. Then, 8.24 g of TEOS were hydrolyzed with TPAOH solution at room temperature for 6 h under stirring (500 rpm). The aluminum source solution was prepared by mixing 0.3 g of $Al(NO_3)_3{\cdot}9H_2O$ and 3.0 g of distilled water at room temperature. Then the $Al(NO_3)_3$ solution was added dropwise to the mixture of TEOS-TPAOH-water with stirring for 3 h. To the resultant homogeneous solution, 90 mg of $SnCl_4{\cdot}5H_2O$ was added with stirring for 30 min, and then 172 μL of Na_2PtCl_4 aqueous (0.34 mol·L^{-1}) and 300 μL of ethylenediamine were added with stirring for another 30 min. The resultant yellow solution was then transferred to Teflon-lined autoclaves and heated in an electric oven at 175 °C for 96 h under static conditions. After the hydrothermal process, the solid product was isolated by centrifugation and washed with distilled water and acetone and then dried at 60 °C. Then the solid sample was calcined under air at 560 °C for 8 h. For the preparation of K-Pd-ZSM5, the only difference was that $SnCl_4{\cdot}5H_2O$ was not added to the synthesis mixture.

Synthesis of K-RhSn-ZSM5. Bimetallic RhSn nanoparticles encapsulated in ZSM5 zeolite with a Si/Al ratio of 50 were prepared by a one-pot synthesis. Batch composition: 1.2 K_2O:16 TPAOH:0.4 Al_2O_3:40 SiO_2:1600 H_2O. First, a TPAOH solution was prepared by mixing 16.24 g of TPAOH (Sigma-Aldrich, 20 wt %, containing ~0.6 wt % of K, product code: 254533-100G) and 12.0 g of distilled water at room temperature. Then, 8.24 g of TEOS were hydrolyzed with TPAOH solution at room temperature for 6 h under stirring (500 rpm). The aluminum source solution was prepared by mixing 0.3 g of $Al(NO_3)_3{\cdot}9H_2O$ and 3.0 g of distilled water at room temperature. Then the $Al(NO_3)_3$ solution was added dropwise to the mixture of TEOS-TPAOH-water with stirring for 3 h. To the resultant homogeneous solution, 90 mg of $SnCl_4{\cdot}5H_2O$ was added with stirring for 30 min, and then 132 μL of $RhCl_3$ aqueous (0.48 mol·L^{-1}) and 300 μL of ethylenediamine were added with stirring for another 30 min. The resultant yellow solution was then transferred to Teflon-lined autoclaves and heated in an electric oven at 175 °C for 96 h under static conditions. After the hydrothermal process, the solid product was isolated by centrifugation and washed with distilled water and acetone and then dried at 60 °C. Then the solid sample was calcined under air at 560 °C for 8 h. For the preparation of K-Rh-ZSM5, the only difference was that $SnCl_4{\cdot}5H_2O$ was not added to the synthesis mixture.

Ion Exchange. Typically, 1 g of sample was dispersed in 30 mL of NH_4Cl aqueous solution (1 mol·L^{-1}) at 80 °C for 6 h under stirring. The solid was collected by centrifugation and washed with deionized water, then the solid was dried at 120 °C for 12 h. The resulting solids were NH_4-type samples. H-type samples were prepared by treating the NH_4-type samples at 400 °C under a H_2 atmosphere for 1 h.

Characterizations

Powder X-ray diffraction was performed with a Rigaku RU-200b powder X-ray diffractometer using Cu Kα radiation. Actual metal contents and Si/Al atomic ratios of the synthetic catalysts were measured by inductively coupled plasma optical emission spectrometry analysis (ICP-OES) on a PerkinElmer Optima 2100DV instrument. A Mettler-Toledo TGA/DSC1 thermogravimetric analyzer was used for the thermogravimetric analysis with a ramping rate of 10 °C·min^{-1} under 50 mL·min^{-1} of air. Coke species on the spent catalysts were observed by Raman spectroscopy using a LabRAM HR800 system at a wavelength of 325 nm. X-ray photoelectron spectroscopy analysis was conducted on a Physical Electronics Company Quantum-2000 Scanning ESCA Microprobe using monochromic Al Kα as an X-ray source. The adventitious carbon C 1s peak (284.8 eV) was used to calibrate the binding energy.

Samples for transmission electron microscopy (TEM) studies were prepared by dropping the suspension of the solid samples in CH_2Cl_2 directly onto holey-carbon-coated copper grids. Electron microscopy measurements were performed using two types of microscopes. Thus, noncorrected JEOL 2100F microscope operating at 200 kV both in transmission and scanning-transmission modes (STEM) was used to record high-angle annular dark-field (HAADF), Z-contrast, images at low resolution. High resolution HAADF-STEM and STEM-iDPC imaging was performed on a double aberration corrected (AC), monochromated, FEI Titan^3 Themis 60-300 microscope working at 300 kV. The iDPC (for integrated-differential phase contrast) imaging provides atomically resolved images in which the contrasts are roughly related to the atomic number of the elements under the beam in thin

https://doi.org/10.1021/jacsau.3c00548
JACS Au 2023, 3, 3213−3226

specimen, instead of the roughly Z^2-dependent contrasts obtained in HAADF-STEM images. By using a four-segment detector, this technique allows imaging light elements, as is the case of O, in the presence of heavier ones (Si, $Z = 14$), which is a key aspect in the atomic scale structural analysis of zeolites. The imaging was conducted under very low electron dose conditions since zeolites are very sensitive to electron beams. In particular, 2048 × 2048 HAADF-iDPC image pairs were recorded simultaneously using a convergence angle of 18.6 mrad and collection angles of 53−198 mrad. This configuration allowed us to optimize the collection of signals on the HAADF and FEI DF4 detectors. In order to limit the damage by the electron beam, a fast image recording protocol was used by combining a beam current of 10−30 pA, a 1.25−2.5 μs dwell time (corresponding to dose rates of 2500−3900 $e^-/Å^2$) and an automated fine-tuning alignment of A1 and C1 using the OptiSTEM software.

X-ray absorption near-edge structure (XANES) and extended X-ray absorption fine structure (EXAFS) at the Pt L_3-edge and Sn K-edge of PtSn-ZSM5 samples were measured at the 20-BM-B beamline of the Advanced Photon Source at Argonne National Laboratory. A Si (111) fixed-exit, double-crystal monochromator was used and the energy resolution was 0.5 eV. Harmonic rejection was facilitated using a Rh-coated mirror (4 mrad) as well as a 15% detuning of the beam intensity at ∼1000 eV above the edge of interest. Data was collected in fluorescence mode using a four elements Vortex Si Drift detector. The samples were prepared as pellets and placed in a furnace with Kapton windows. The PtSn-ZSM5 samples were in situ reduced by H_2 at 600 °C and then cooled to room temperature before the Pt L_3-edge and Sn K-edge EXAFS spectra were recorded at room temperature.

The infrared spectroscopy studies were carried out on a Bruker VERTEX 70 infrared spectrometer. When IR spectra upon CD_3CN adsorption were collected, 30 mg of each sample was pressed into self-supported thin pallets followed by pretreatment at 400 °C for 1 h under vacuum before cooling to room temperature. The samples were then saturated with deuterated acetonitrile vapor until equilibrated. The spectra of the samples were recorded continuously during evacuation until physically adsorbed CD_3CN was completely removed. When collecting IR spectra in the −OH stretching region of catalysts, 30 mg of each sample was pressed into self-supporting thin pallets. The samples were then pretreated at 400 °C for 1 h under vacuum to remove adsorbed water, and the spectra were recorded after cooling to room temperature. When collecting IR spectra upon pyridine adsorption, 30 mg of each sample was pressed into self-supported thin pallets and pretreated at 350 °C for 0.5 h under vacuum followed by cooling to room temperature. Subsequently, samples were saturated with pyridine vapor until equilibrium. Finally, pyridine was desorbed at 200 °C for 0.5 h and the spectra were measured after cooling to room temperature.

Solid state ^{31}P magic angle spinning nuclear magnetic resonance (MAS NMR) spectra were acquired after adsorption of trimethylphosphine oxide (TMPO, Alfa Aesar, 99%) using a 600 a Bruker Advance III spectrometer. First, the samples were degassed for 20 h under dynamic vacuum at 420 °C to remove any adsorbed water. Samples were thereafter transferred to a glovebox to prevent exposing them to moisture. Subsequently, 1 mL of dichloromethane solution containing TMPO (0.2 wt %) was added into 150 mg of samples followed by string at room temperature for 2 h. Samples dosed with TMPO were pack into zirconia MAS NMR rotors in glovebox after volatilization of dichloromethane. The chemical shifts were referenced to ammonium dihydrogen phosphate at 1.1 ppm.

Catalytic Evaluation

Ethene and *cis*-Cyclooctene Hydrogenation. The hydrogenation reaction was carried out in a 250 mL stainless-steel autoclave. With regard to hydrogenation of ethene, catalysts (10 mg) were added into the autoclave, followed by introducing the feed gas containing 0.1 MPa ethene and 0.3 MPa H_2. For hydrogenation of *cis*-cyclooctene, 10 mg of catalysts, 0.6 g of *cis*-cyclooctene, and 1 g of cyclohexane (as a solvent) were mixed in the autoclave followed by introducing 5 MPa H_2. The hydrogenation rates were measured at 80 °C under vigorous agitation at 800 rpm. The r_{ethene} and $r_{cis-cyclooctene}$ values were defined as moles of olefin converted per mole of Pt per hour.

Alkylation of Benzene with Ethane. This reaction was carried out in a fixed-bed reactor at atmospheric pressure and 400 °C. Typically, 200 mg of NH_4-type Pt-zeolite catalyst with 40−60 mesh particle size was loaded into the reaction tube. Before the reaction, the catalyst was treated by H_2 flow (35 mL·min^{-1}) at 400 °C for 1 h with a ramping rate of 10 °C·min^{-1}. Subsequently, the reaction was carried out with a molar ratio of ethane to benzene of 9 and weight hour space velocity (WHSV) of ethane at 2.0 h^{-1}. For the long-term stability test of PtSn-HZSM5, 300 mg of catalyst and WHSV of ethane at 1.2 h^{-1} were used. All products were analyzed using an online gas chromatograph that can detect alkanes, alkenes and aromatics. The line between the reaction tube and the gas chromatograph was kept at 180 °C to prevent condensation of the products. The ethane conversion (X_{ethane}) and benzene conversion ($X_{benzene}$) are calculated as follows:

$$X_{ethane} = \frac{\sum f_i n_i A_i - f_{ethane} n_{ethane} A_{ethane}}{\sum f_i n_i A_i}$$

$$X_{benzene} = \frac{\sum f_j n_j A_j - f_{benzene} n_{benzene} A_{benzene}}{\sum f_j n_j A_j}$$

For all products, their selectivity (S_i) calculated based on ethane is defined as

$$S_i = \frac{f_i n_i A_i}{\sum f_i n_i A_i - f_{ethane} n_{ethane} A_{ethane}}$$

For the aromatic product, their selectivity (S_j) calculated based on benzene is defined as

$$S_j = \frac{f_j n_j A_j}{\sum f_j n_j A_j - f_{benzene} n_{benzene} A_{benzene}}$$

where f_i and f_j are the mole correction factors of compounds, A_i and A_j are the peak areas of compounds, n_i is the carbon number of chain hydrocarbons and branched chain of aromatics, and n_j is the carbon number of phenyl ring of aromatics.

Alkylation of Benzene with Ethene. This reaction was carried out in a fixed-bed reactor at atmospheric pressure and 400 °C. Typically, 150 mg of NH_4-type zeolite catalyst with 40−60 mesh particle sizes was loaded into the reaction tube. Before the reaction, the catalyst was treated by H_2 flow (35 mL·min^{-1}) at 400 °C for 1 h with a ramping rate of 10 °C·min−1. Subsequently, the reaction was carried out with a molar ratio of benzene to ethene of 2 and WHSV of ethene at 0.55 h^{-1}. All products were analyzed using an online gas chromatograph that can detect alkanes, alkenes and aromatics. The line between the reaction tube and the gas chromatograph was kept at 180 °C to prevent condensation of the products. The ethene conversion (X_{ethene}) and benzene conversion ($X_{benzene}$) are calculated as follows:

$$X_{ethene} = \frac{\sum f_i n_i A_i - f_{ethene} n_{ethene} A_{ethene}}{\sum f_i n_i A_i}$$

$$X_{benzene} = \frac{\sum f_j n_j A_j - f_{benzene} n_{benzene} A_{benzene}}{\sum f_j n_j A_j}$$

where f_i and f_i are the mole correction factors of compounds. A_i and A_i are the peak areas of compounds. n_i is the carbon number of chain hydrocarbons and the branched chain of aromatics, and n_j is the carbon number of phenyl ring of aromatics.

H/D Exchange. The H/D exchange between ethane and D_2 was performed on a CatLab (Hiden, UK) instrument equipped with a mass spectrometer. Typically, 20 mg of sample was loaded in a quart

https://doi.org/10.1021/jacsau.3c00548
JACS Au 2023, 3, 3213−3226

tube and prereduced by H_2 for 1 h at 400 °C followed by cooling to 40 °C. Then, the gas flow was switched into a mixture containing 1 mL·min^{-1} ethane and 16 mL·min^{-1} D_2. Subsequently, the temperature was heated to 400 °C with a ramping rate of 10 °C·min^{-1} and the outlet gas was analyzed with a mass spectrometer.

■ ASSOCIATED CONTENT

Supporting Information

The Supporting Information is available free of charge at https://pubs.acs.org/doi/10.1021/jacsau.3c00548.

Chemical compositions of the metal-zeolite materials, electron microscopy and spectroscopy results of the metal-zeolite materials, results of catalytic tests, characterizations of the spent catalysts and summary of the catalytic performances reported in the literature works (PDF)

■ AUTHOR INFORMATION

Corresponding Authors

Lichen Liu − *Department of Chemistry, Tsinghua University, Beijing 100084, China;* orcid.org/0000-0001-5067-0481; Email: lichenliu@mail.tsinghua.edu.cn

Peng He − *State Key Laboratory of Coal Conversion, Institute of Coal Chemistry, Chinese Academy of Sciences, Taiyuan 030001, China; National Energy Center for Coal to Clean Fuels, Synfuels China Technology Co., Ltd., Beijing 101407, China; University of Chinese Academy of Sciences, Beijing 00049, China;* orcid.org/0000-0002-7141-4660; Email: hepeng@sxicc.ac.cn

Authors

Kun Zhang − *State Key Laboratory of Coal Conversion, Institute of Coal Chemistry, Chinese Academy of Sciences, Taiyuan 030001, China; University of Chinese Academy of Sciences, Beijing 00049, China;* orcid.org/0009-0008-8713-8497

Xiaomeng Dou − *Department of Chemistry, Tsinghua University, Beijing 100084, China*

Huaming Hou − *National Energy Center for Coal to Clean Fuels, Synfuels China Technology Co., Ltd., Beijing 101407, China*

Ziyu Zhou − *State Key Laboratory of Coal Conversion, Institute of Coal Chemistry, Chinese Academy of Sciences, Taiyuan 030001, China; University of Chinese Academy of Sciences, Beijing 00049, China*

Miguel Lopez-Haro − *Departamento de Ciencia de los Materiales e Ingeniería Metalúrgica y Química Inorgánica, Facultad de Ciencias, Universidad de Cádiz, Puerto Real, Cádiz 11519, Spain;* orcid.org/0000-0003-2560-8015

Debora M. Meira − *CLS@APS sector 20, Advanced Photon Source, Argonne National Laboratory, Argonne, Illinois 60439, United States; Canadian Light Source Inc., Saskatoon, Saskatchewan S7N 2V3, Canada;* orcid.org/0000-0002-7529-2736

Ping Liu − *State Key Laboratory of Coal Conversion, Institute of Coal Chemistry, Chinese Academy of Sciences, Taiyuan 030001, China*

Complete contact information is available at: https://pubs.acs.org/10.1021/jacsau.3c00548

Author Contributions

†K.Z., X.D., and H.H. contributed equally. CRediT: **Kun Zhang** data curation, formal analysis, investigation, writing-original draft; **Xiaomeng Dou** data curation, formal analysis, investigation, methodology; **Huaming Hou** investigation; **Ziyu Zhou** data curation, formal analysis; **Debora Motta Meira** investigation; **Ping Liu** formal analysis; **Peng He** conceptualization, funding acquisition, investigation, project administration, writing-review & editing; **Lichen Liu** conceptualization, funding acquisition, project administration, supervision, writing-original draft, writing-review & editing.

Notes

The authors declare no competing financial interest.

■ ACKNOWLEDGMENTS

P.H. and L.L. acknowledges the National Natural Science Foundation of China (22002179 and 22272087). L.L. thanks the financial supports from Tsinghua University (Initiative Scientific Research Program 20211080079 and Dushi Program 20231080010) and the Foundation of State Key Laboratory of Coal Conversion (J22-23-602). M.L.-H. thanks the financial support from MCIN/AEI/10.13039/501100011033 (PID2019-110018GA-I00). This research used resources of the Advanced Photon Source, an Office of Science User Facility operated for the U.S. Department of Energy (DOE) Office of Science by Argonne National Laboratory, and was supported by the U.S. DOE under Contract No. DE-AC02-06CH11357, and the Canadian Light Source and its funding partners.

■ REFERENCES

(1) Liu, L.; Corma, A. Confining isolated atoms and clusters in crystalline porous materials for catalysis. *Nat. Rev. Mater.* **2021**, *6*, 244−263.

(2) Sun, Q.; Wang, N.; Yu, J. Advances in Catalytic Applications of Zeolite-Supported Metal Catalysts. *Adv. Mater.* **2021**, *33*, No. e2104442.

(3) Babucci, M.; Guntida, A.; Gates, B. C. Atomically Dispersed Metals on Well-Defined Supports including Zeolites and Metal-Organic Frameworks: Structure, Bonding, Reactivity, and Catalysis. *Chem. Rev.* **2020**, *120*, 11956−11985.

(4) Peng, M.; Dong, C.; Gao, R.; Xiao, D.; Liu, H.; Ma, D. Fully Exposed Cluster Catalyst (FECC): Toward Rich Surface Sites and Full Atom Utilization Efficiency. *ACS Cent. Sci.* **2021**, *7*, 262−273.

(5) Liu, L.; Corma, A. Metal Catalysts for Heterogeneous Catalysis: From Single Atoms to Nanoclusters and Nanoparticles. *Chem. Rev.* **2018**, *118*, 4981−5079.

(6) Liu, L.; Diaz, U.; Arenal, R.; Agostini, G.; Concepcion, P.; Corma, A. Generation of subnanometric platinum with high stability during transformation of a 2D zeolite into 3D. *Nat. Mater.* **2017**, *16*, 132−138.

(7) Liu, L.; Lopez-Haro, M.; Lopes, C. W.; Li, C.; Concepcion, P.; Simonelli, L.; Calvino, J. J.; Corma, A. Regioselective generation and reactivity control of subnanometric platinum clusters in zeolites for high-temperature catalysis. *Nat. Mater.* **2019**, *18*, 866−873.

(8) Clatworthy, E. B.; Konnov, S. V.; Dubray, F.; Nesterenko, N.; Gilson, J. P.; Mintova, S. Emphasis on the Properties of Metal-Containing Zeolites Operating Outside the Comfort Zone of Current Heterogeneous Catalytic Reactions. *Angew. Chem., Int. Ed.* **2020**, *59*, 19414−19432.

(9) Zhang, Q.; Gao, S.; Yu, J. Metal Sites in Zeolites: Synthesis, Characterization, and Catalysis. *Chem. Rev.* **2023**, *123*, 6039−6106.

(10) Wang, H.; Wang, L.; Xiao, F. S. Metal@Zeolite Hybrid Materials for Catalysis. *ACS Cent. Sci.* **2020**, *6*, 1685−1697.

(11) Chai, Y.; Shang, W.; Li, W.; Wu, G.; Dai, W.; Guan, N.; Li, L. Noble Metal Particles Confined in Zeolites: Synthesis, Characterization, and Applications. *Adv. Sci.* **2019**, *6*, 1900299.
(12) Choi, M.; Wu, Z.; Iglesia, E. Mercaptosilane-assisted synthesis of metal clusters within zeolites and catalytic consequences of encapsulation. *J. Am. Chem. Soc.* **2010**, *132*, 9129−9137.
(13) Moliner, M.; Gabay, J. E.; Kliewer, C. E.; Carr, R. T.; Guzman, J.; Casty, G. L.; Serna, P.; Corma, A. Reversible Transformation of Pt Nanoparticles into Single Atoms inside High-Silica Chabazite Zeolite. *J. Am. Chem. Soc.* **2016**, *138*, 15743−15750.
(14) Zhang, J.; Wang, L.; Zhang, B.; Zhao, H.; Kolb, U.; Zhu, Y.; Liu, L.; Han, Y.; Wang, G.; Wang, C.; et al. Sinter-resistant metal nanoparticle catalysts achieved by immobilization within zeolite crystals via seed-directed growth. *Nat. Catal.* **2018**, *1*, 540−546.
(15) Cho, H. J.; Kim, D.; Li, J.; Su, D.; Xu, B. Zeolite-Encapsulated Pt Nanoparticles for Tandem Catalysis. *J. Am. Chem. Soc.* **2018**, *140*, 13514−13520.
(16) Goel, S.; Wu, Z.; Zones, S. I.; Iglesia, E. Synthesis and catalytic properties of metal clusters encapsulated within small-pore (SOD, GIS, ANA) zeolites. *J. Am. Chem. Soc.* **2012**, *134*, 17688−17695.
(17) Goel, S.; Zones, S. I.; Iglesia, E. Encapsulation of metal clusters within MFI via interzeolite transformations and direct hydrothermal syntheses and catalytic consequences of their confinement. *J. Am. Chem. Soc.* **2014**, *136*, 15280−15290.
(18) Felvey, N.; Guo, J.; Rana, R.; Xu, L.; Bare, S. R.; Gates, B. C.; Katz, A.; Kulkarni, A. R.; Runnebaum, R. C.; Kronawitter, C. X. Interconversion of Atomically Dispersed Platinum Cations and Platinum Clusters in Zeolite ZSM-5 and Formation of Platinum gem-Dicarbonyls. *J. Am. Chem. Soc.* **2022**, *144*, 13874−13887.
(19) Cundy, C. S.; Cox, P. A. The hydrothermal synthesis of zeolites: Precursors, intermediates and reaction mechanism. *Microporous Mesoporous Mater.* **2005**, *82*, 1−78.
(20) *Database of Zeolite Structures*: International Zeolite Association. http://www.iza-structure.org/databases/.
(21) Čejka, J.; Corma, A.; Zones, S. *Zeolites and Catalysis: Synthesis, Reactions and Applications*; Wiley-VCH Verlag GmbH & Co. KGaA, 2010.
(22) Park, K.-C.; Ihm, S.-K. Comparison of Pt/zeolite catalysts for n-hexadecane hydroisomerization. *Appl. Catal. A: Gen.* **2000**, *203*, 201−209.
(23) Suárez, N.; Arribas, M. A.; Moreno, A.; Martínez, A. High-performing Ir- and Pt-containing catalysts based on mesoporous beta zeolite for the selective ring opening of decalin. *Catal. Sci. Technol.* **2020**, *10*, 1073−1085.
(24) Liu, L. C.; Lopez-Haro, M.; Lopes, C. W.; Rojas-Buzo, S.; Concepcion, P.; Manzorro, R.; Simonelli, L.; Sattler, A.; Serna, P.; Calvino, J. J.; et al. Structural modulation and direct measurement of subnanometric bimetallic PtSn clusters confined in zeolites. *Nat. Catal.* **2020**, *3*, 628−638.
(25) Liu, L.; Lopez-Haro, M.; Perez-Omil, J. A.; Boronat, M.; Calvino, J. J.; Corma, A. Direct assessment of confinement effect in zeolite-encapsulated subnanometric metal species. *Nat. Commun.* **2022**, *13*, 821.
(26) Hou, D.; Grajciar, L.; Nachtigall, P.; Heard, C. J. Origin of the Unusual Stability of Zeolite-Encapsulated Sub-Nanometer Platinum. *ACS Catal.* **2020**, *10*, 11057−11068.
(27) Hernandez-Tamargo, C. E.; Roldan, A.; de Leeuw, N. H. A density functional theory study of the structure of pure-silica and aluminium-substituted MFI nanosheets. *J. Solid State Chem.* **2016**, *237*, 192−203.
(28) Liu, L.; Zakharov, D. N.; Arenal, R.; Concepcion, P.; Stach, E. A.; Corma, A. Evolution and stabilization of subnanometric metal species in confined space by in situ TEM. *Nat. Commun.* **2018**, *9*, 574.
(29) Shinjoh, H.; Hatanaka, M.; Nagai, Y.; Tanabe, T.; Takahashi, N.; Yoshida, T.; Miyake, Y. Suppression of Noble Metal Sintering Based on the Support Anchoring Effect and its Application in Automotive Three-Way Catalysis. *Top. Catal.* **2009**, *52*, 1967−1971.
(30) Jones, J.; Xiong, H.; DeLaRiva, A. T.; Peterson, E. J.; Pham, H.; Challa, S. R.; Qi, G.; Oh, S.; Wiebenga, M. H.; Pereira Hernandez, X. I.; et al. Thermally stable single-atom platinum-on-ceria catalysts via atom trapping. *Science* **2016**, *353*, 150−154.
(31) Thang, H. V.; Pacchioni, G.; DeRita, L.; Christopher, P. Nature of stable single atom Pt catalysts dispersed on anatase TiO_2. *J. Catal.* **2018**, *367*, 104−114.
(32) Xu, Y.; Zheng, W.; Liu, X.; Zhang, L.; Zheng, L.; Yang, C.; Pinna, N.; Zhang, J. Platinum single atoms on tin oxide ultrathin films for extremely sensitive gas detection. *Mater. Horizons* **2020**, *7*, 1519−1527.
(33) Liu, L.; Lopez-Haro, M.; Calvino, J. J.; Corma, A. Tutorial: structural characterization of isolated metal atoms and subnanometric metal clusters in zeolites. *Nat. Protoc.* **2021**, *16*, 1871−1906.
(34) Yokoi, T.; Mochizuki, H.; Namba, S.; Kondo, J. N.; Tatsumi, T. Control of the Al Distribution in the Framework of ZSM-5 Zeolite and Its Evaluation by Solid-State NMR Technique and Catalytic Properties. *J. Phys. Chem. C* **2015**, *119*, 15303−15315.
(35) Wragg, D. S.; Morris, R. E.; Burton, A. W. Pure Silica Zeolite-type Frameworks: A Structural Analysis. *Chem. Mater.* **2008**, *20*, 1561−1570.
(36) Liu, S.; Wu, X.; Luo, H.; Weng, D.; Ran, R. Pt/Zeolite Catalysts for Soot Oxidation: Influence of Hydrothermal Aging. *J. Phys. Chem. C* **2015**, *119*, 17218−17227.
(37) Liu, M.; Tang, W.; Xie, Z.; Yu, H.; Yin, H.; Xu, Y.; Zhao, S.; Zhou, S. Design of Highly Efficient Pt-SnO_2 Hydrogenation Nanocatalysts using Pt@Sn Core-Shell Nanoparticles. *ACS Catal.* **2017**, *7*, 1583−1591.
(38) Harris, J. W.; Cordon, M. J.; Di Iorio, J. R.; Vega-Vila, J. C.; Ribeiro, F. H.; Gounder, R. Titration and quantification of open and closed Lewis acid sites in Sn-Beta zeolites that catalyze glucose isomerization. *J. Catal.* **2016**, *335*, 141−154.
(39) Zheng, A.; Huang, S. J.; Liu, S. B.; Deng, F. Acid properties of solid acid catalysts characterized by solid-state ^{31}P NMR of adsorbed phosphorous probe molecules. *Phys. Chem. Chem. Phys.* **2011**, *13*, 14889−14901.
(40) Wang, Y.; Xin, S.; Chu, Y.; Xu, J.; Qi, G.; Wang, Q.; Xia, Q.; Deng, F. Influence of Trimethylphosphine Oxide Loading on the Measurement of Zeolite Acidity by Solid-State NMR Spectroscopy. *J. Phys. Chem. C* **2021**, *125*, 9497−9506.
(41) Liu, L.; Lopez-Haro, M.; Lopes, C. W.; Rojas-Buzo, S.; Concepcion, P.; Manzorro, R.; Simonelli, L.; Sattler, A.; Serna, P.; Calvino, J. J.; et al. Structural modulation and direct measurement of subnanometric bimetallic PtSn clusters confined in zeolites. *Nat. Catal.* **2020**, *3*, 628−638.
(42) Lewis, J. D.; Ha, M.; Luo, H.; Faucher, A.; Michaelis, V. K.; Román-Leshkov, Y. Distinguishing Active Site Identity in Sn-Beta Zeolites Using 31P MAS NMR of Adsorbed Trimethylphosphine Oxide. *ACS Catal.* **2018**, *8*, 3076−3086.
(43) Cho, H. J.; Dornath, P.; Fan, W. Synthesis of Hierarchical Sn-MFI as Lewis Acid Catalysts for Isomerization of Cellulosic Sugars. *ACS Catal.* **2014**, *4*, 2029−2037.
(44) Gabrienko, A. A.; Danilova, I. G.; Arzumanov, S. S.; Toktarev, A. V.; Freude, D.; Stepanov, A. G. Strong acidity of silanol groups of zeolite beta: Evidence from the studies by IR spectroscopy of adsorbed CO and 1H MAS NMR. *Microporous Mesoporous Mater.* **2010**, *131*, 210−216.
(45) Lønstad Bleken, B. T.; Mino, L.; Giordanino, F.; Beato, P.; Svelle, S.; Lillerud, K. P.; Bordiga, S. Probing the surface of nanosheet H-ZSM-5 with FTIR spectroscopy. *Phys. Chem. Chem. Phys.* **2013**, *15*, 13363−13370.
(46) Yuan, Y.; Lobo, R. F.; Xu, B. Ga2O22+ Stabilized by Paired Framework Al Atoms in MFI: A Highly Reactive Site in Nonoxidative Propane Dehydrogenation. *ACS Catal.* **2022**, *12*, 1775−1783.
(47) Almutairi, S. M. T.; Mezari, B.; Magusin, P. C. M. M.; Pidko, E. A.; Hensen, E. J. M. Structure and Reactivity of Zn-Modified ZSM-5 Zeolites: The Importance of Clustered Cationic Zn Complexes. *ACS Catal.* **2012**, *2*, 71−83.
(48) Xu, Z.; Yue, Y.; Bao, X.; Xie, Z.; Zhu, H. Propane Dehydrogenation over Pt Clusters Localized at the Sn Single-Site in Zeolite Framework. *ACS Catal.* **2020**, *10*, 818−828.

https://doi.org/10.1021/jacsau.3c00548
JACS Au 2023, 3, 3213−3226

(49) Vazhnova, T.; Rigby, S. P.; Lukyanov, D. B. Benzene alkylation with ethane in ethylbenzene over a PtH-MFI catalyst: Kinetic and IR investigation of the catalyst deactivation. *J. Catal.* **2013**, *301*, 125−133.
(50) Chua, L. M.; Vazhnova, T.; Mays, T. J.; Lukyanov, D. B.; Rigby, S. P. Deactivation of PtH-MFI bifunctional catalysts by coke formation during benzene alkylation with ethane. *J. Catal.* **2010**, *271*, 401−412.

https://doi.org/10.1021/jacsau.3c00548
JACS Au 2023, 3, 3213−3226